Characterizing topological transitions in a Turing-pattern-forming reaction-diffusion system

Jacobo Guiu-Souto,* Jorge Carballido-Landeira, and Alberto P. Muñuzuri
Group of Nonlinear Physics, Department of Physics, University of Santiago de Compostela, E-15782 Santiago de Compostela, Spain
(Received 19 September 2011; revised manuscript received 3 February 2012; published 10 May 2012)

Turing structures appear naturally and they are demonstrated under different spatial configurations such as stripes and spots as well as mixed states. The traditional tool to characterize these patterns is the Fourier transformation, which accounts for the spatial wavelength, but it fails to discriminate among different spatial configurations or mixed states. In this paper, we propose a parameter that clearly differentiates the different spatial configurations. As an application, we considered the transitions induced by an external forcing in a reaction-diffusion system although the results are straightforwardly extended to different problems with similar topologies. The method was also successfully tested on a temporally evolving pattern.

DOI: 10.1103/PhysRevE.85.056205 PACS number(s): 05.45.−a, 05.20.−y, 47.54.−r, 82.33.Nq

I. INTRODUCTION

Turing instability [1] has been proposed to understand and reproduce pattern formation mechanisms underlying a great variety of structures in nature [2–4]. Turing structures are stationary patterns that may appear when propagating chemical waves [5] are combined with diffusive effects. Over the past few decades, several authors [6–9] have shown that Turing instability represents a good mechanism to understand pattern formation from a physicochemical point of view.

In general, two-dimensional Turing patterns may spontaneously appear under three completely different spatial configurations, namely hexagonal arrangement of spots, stripes (or labyrinthine configuration), and reverse hexagons. A summary of these patterns is shown in Fig. 1. Note that it is possible to consider direct (white) or reverse (black) stripes depending on whether the background is black or white, respectively (see Fig. 1). Turing structures have been thoroughly studied in different reaction-diffusion systems, such as the chlorite-dioxide-iodine-malonic acid (CDIMA) reaction [10–13] and the Belousov-Zhabotinsky reaction confined to water-in-oil aerosol AOT microemulsions (BZ-AOT) [14–16]. In an attempt to reproduce forcing effects on patterns in nature, Turing patterns are frequently studied in the presence of external perturbations [17–23].

The usual approach to describe and characterize such complex spatial structures is the two-dimensional Fourier transform, which provides useful information (length scales or orientation order) in cases of regular structures. However, this technique is unable to differentiate the topology of black spots from that of white spots [as shown in the insets in Figs. 1(a) and 1(d)], providing only information about the length scale by the wave number. Moreover, the Fourier transform clearly fails to identify mixed states as we show in Figs. 1(b) and 1(c). This problem becomes more crucial when the pattern is endowed with dynamics and spontaneously transits from one type to another [24,25]. In this latest case, there is a necessity to implement a parameter that straightforwardly characterizes the transitions.

In order to easily distinguish among different Turing structures, we introduce in this paper a set of quantitative morphological measures that describe the geometrical and topological properties of Turing patterns, i.e., area, boundary length, cluster numbering, connectivity, and so on. Some of these morphological measures are defined as Minkowski functionals [26–28], which are well known in mathematical morphology [29] and in image analysis [30]. These measures have been already applied in other physical systems where spatial patterns play an important role, such as the description of microemulsions [31], the scale distribution of galaxies in the universe [32], and percolation in porous media [33], to mention just a few. We analyze the meaning of these measures within our context and define a single parameter that contains all topological relevant information for our patterns. It allows us to discriminate all the different patterns exhibited by the system as well as to identify the transitions that may undergo.

This paper is organized as follows. In Sec. II we introduce the reaction-diffusion model that is used in the paper. Section III describes in detail the morphological measures. The results of the morphological analysis applied to our system are presented in Sec. IV. Section V presents the conclusions and discussion.

II. NUMERICAL SIMULATIONS

A. Model

To exemplify and illustrate the meaning of the functionals described in this paper we considered the patterns obtained from the simulations as described below.

A theoretical model [34] that is commonly accepted to describe the formation of Turing patterns in a chemical system (BZ-AOT reaction [35–37]) is the two-variable Oregonator-like model,

$$\frac{\partial c_1}{\partial t} = \frac{1}{\varepsilon}\left[f c_2 \frac{q - c_1}{q + c_1} + c_1 \frac{1 - m c_2}{1 - m c_2 + \varepsilon_1} - c_1^2 \right] + D_1 \nabla^2 c_1, \tag{1}$$

$$\frac{\partial c_2}{\partial t} = c_1 \frac{1 - m c_2}{1 - m c_2 + \varepsilon_1} - c_2 + D_2 \nabla^2 c_2, \tag{2}$$

where c_1 and c_2 are parameters related to the concentrations of the main species competing in the pattern formation mechanism known as the activator and inhibitor, respectively, and D_1, D_2 are their corresponding diffusion coefficients. The parameters f, m, q, ε_1, and ε depend on the reaction rates and

*Corresponding author: jacobo.guiu@usc.es

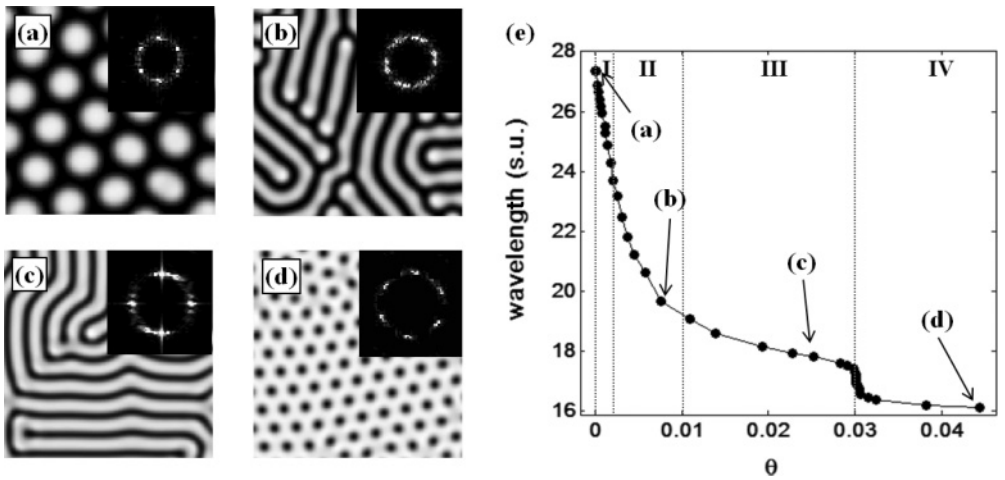

FIG. 1. Numerical simulation of Turing patterns modeled by Eqs. (1) and (2), including different forcing by using Eqs. (4) and (5). The parameters of the model were kept constant: $f = 1.2$, $m = 190$, $q = 0.001$, $\varepsilon_1 = 0.01$, $\varepsilon = 0.01$, and $d_0 = 0.01$. The computational domain consists in a two-dimensional mesh of 300 × 300 grid points, with a spatial step of 0.1 s.u. (space units). We integrate using a fully explicit three-level algorithm with a temporal step of 0.001 t.u. (time units). (a) Hexagonal pattern (white spots) in the absence of forcing ($\Theta = 0$). (b) Direct labyrinthine structure (white stripes) at $\Theta = 0.008$. (c) Reverse labyrinthine structure (black stripes) at $\Theta = 0.025$. (d) Reverse hexagons (black spots) at $\Theta = 0.045$. (e) Dependence of the Turing wavelength, obtained by using the Fourier transform, as a function of the control parameter Θ. Regions I ($\Theta = 0$–0.0025), II ($\Theta = 0.0025$–0.01), III ($\Theta = 0.01$–0.03), and IV ($\Theta = 0.03$–0.045) correspond with white spots, white stripes, black stripes, and black spots, respectively.

they appear as a result of applying the mass action law on the chemical equations and *a posteriori* dimensionless analysis [38] (appropriated values to model the BZ-AOT system are $f = 1.2$, $m = 190$, $q = 0.001$, $\varepsilon_1 = 0.01$, and $\varepsilon = 0.01$).

The main example considered in this paper is given by Eqs. (1) and (2) under external perturbation. Here we considered a case previously discussed elsewhere that basically modulates the gravity periodically. As discussed in Refs. [35,39] the effect of this external forcing results in a modification of the effective diffusion coefficient [40] for the different species involved as follows:

$$D_{1,2} = \frac{D^0_{1,2}(\beta, m_{1,2})}{3\sqrt{3}}(3 + \beta m_{1,2}\omega^2 A^2)^{3/2}, \tag{3}$$

where $D^0_{1,2}$ are the diffusion coefficients of the free particles, $m_{1,2}$ are the masses of the two species involved, ω and A are the frequency and amplitude of the harmonic forcing, and $\beta = 1/K_B T$, where K_B is the Boltzmann constant. Taking into account that $m_1 = K m_2$, with $K \sim 1000$ [34,35], we can obtain a more compact expression,

$$d \equiv \frac{D_1}{D_2} = d_0 \left(1 + \frac{K - 1}{1 + \frac{3}{\Theta}}\right)^{3/2}, \tag{4}$$

where d_0 is the ratio between the diffusion coefficients in the absence of forcing and Θ is a non-dimensional factor proportional to the perturbation defined by

$$\Theta = \beta m_2 \omega^2 A^2, \tag{5}$$

which plays the role of a control parameter in our case.

B. Simulations

In order to obtain the different patterns, we solve the reaction-diffusion Eqs. (1) and (2) with the modified diffusion coefficients obtained through Eqs. (3) and (4). We consider $d_0 = 0.01$ (with $D_1 = 1$) as the ratio between the diffusion coefficients in the free-of-forcing case. As initial conditions we considered random noise and zero flux boundary conditions. We integrate the equations using a fully explicit three-level Du Fort-Frankel scheme [41] with a spatial step of 0.1 s.u. (space units).

Depending on the control parameter Θ, the system was able to experience transitions from one type of pattern to another. In Fig. 1 we present the four representative cases where variations of the control parameter induce different arrangements of Turing structures. In particular, region I ($\Theta =$ 0–0.0025) shows a hexagonal Turing pattern in the absence of forcing [Fig. 1(a)] and region II ($\Theta =$ 0.0025–0.01) exhibits a labyrinth structure [Fig. 1(b)]. By smoothly increasing the forcing, from $\Theta =$ 0.01–0.03 (region III), the labyrinth is more connected, until the white pattern dominates over the black background [Fig. 1(c)]. From this point of view these patterns obtained in region III can be considered as a reverse labyrinth. Higher values of the forcing ($\Theta =$ 0.03–0.045) show reverse hexagons (region IV), as shown in Fig. 1(d). For values of forcing larger than $\Theta = 0.045$, the system undergoes a Hopf bifurcation and becomes oscillatory. By analyzing the fast Fourier transform we observed that the transition from white spots to reverse labyrinthine shows a large decrease in the wavelength, in contrast with the smooth changes observed in the black hexagonal spots regime, as can be observed in Fig. 1(e).

C. Obtaining the discrete image

In order to analyze the different parameters that may be suitable to morphologically characterize our patterns, we need

to transform the grayscale images from simulations into black-and-white discrete images. This step uses the Otsu algorithm [42] that considers as white pixels, n^w, those with a gray level larger than one established value, ρ, usually taken at full width at half maximum (FWHM) of the gray scale, and the rest of the pixels are considered black pixels, n^b. It is important to note that, if ρ is equal to the maximum (minimum) of the gray level, all pixels are considered black (white), according to this algorithm.

Figure 2 shows an example illustrating the preceding procedure. We take a portion of the black-spots pattern from Fig. 1(d) (in gray scale) and then apply the Otsu algorithm.

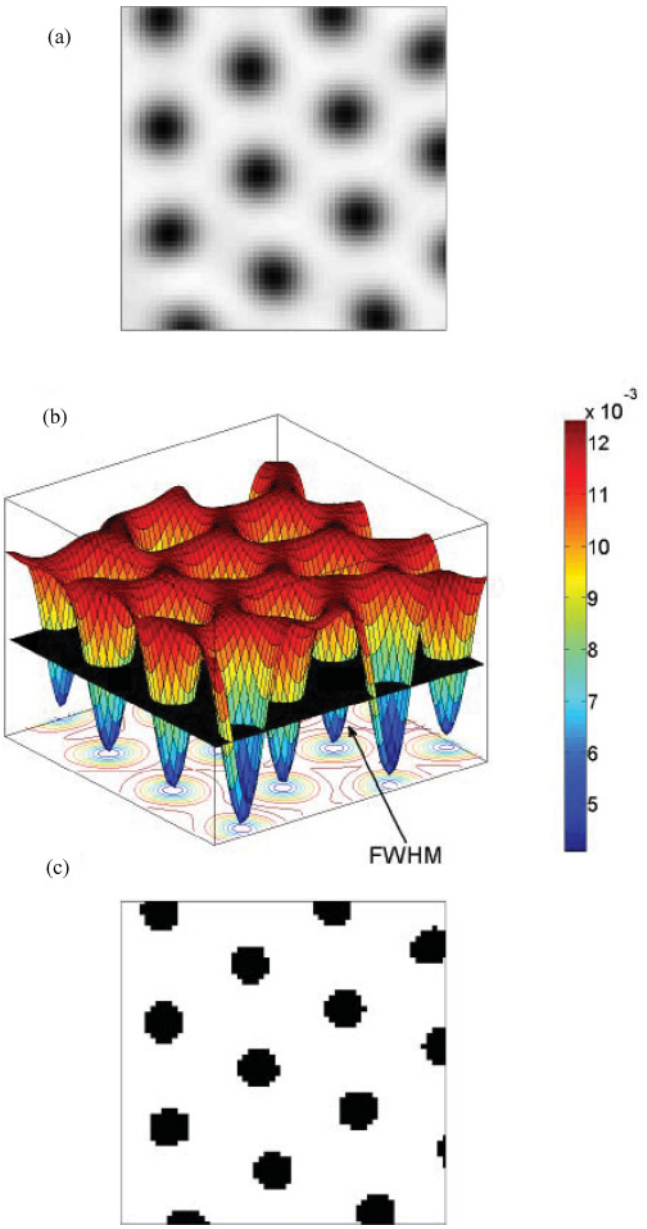

FIG. 2. (Color online) Transformation of a gray scale image into a discrete image. (a) Gray scale image corresponding with a portion (80 × 80 pixels) of the black spots shown in Fig. 1(d). (b) 3D representation of the gray scale image with the plane corresponding at FWHM to make the binarization of the image. (c) Resulting discrete image, with the black and white pixels configuration.

The result is plotted in three dimensions in Fig. 2(b), where we fix the plane corresponding with the FWHM. The result is a discrete image as shown in Fig. 2(c), basically composed of white and black pixels.

III. MORPHOLOGICAL MEASURES

In the previous section, we considered a mechanism able to modify the type of Turing pattern depending on a control parameter Θ. We now are going to study these transitions from a morphological point of view. In this regard, we introduce a set of morphological measures to analyze the Turing patterns, some of which belong to the Minkowski functionals [26]. These measures are able to characterize the geometry and topology of the black-and-white discrete images.

The first measure to describe the black-and-white pattern morphology is the area, A^w; this is the number of white pixels, n^w, in the discrete image. Note that knowing n^w directly yields the total number of black pixels by $n^b = N - n^w$, where N is the total number of pixels (in our example $N = 300 \times 300$). The second functional is the boundary length or the perimeter, B, which separates the black and white regions in the discrete image [see Fig. 2(c) to observe the black and white regions].

Another morphological quantity is the number of white (black) clusters C^w (C^b) present in the patterns. Moreover, we can also estimate the eccentricity of each cluster by means of an ellipse that has the same normalized second central moment as the cluster [43]. We then calculate the mean eccentricity (ε^w and ε^b corresponding to the white and black clusters, respectively). Note that an eccentricity close to zero indicates that the cluster is a circle, whereas, for a value close to 1, the cluster resembles a segment.

The following functional is the Euler number, E, that contains only topological information. It measures the connectivity of the black and white regions. Despite the global definition of the Euler number, there are different ways to calculate this parameter. The first one, E_1, considers the Euler number defined as $E_1 = (n^w - n^b)/N$. According to this, if this quantity takes values lower (larger) than zero the black (white) area dominates. In this way, this is a good measure to differentiate direct and reverse structures. The other definition, E_2, counts the number of white clusters or islands (black holes) over the black (white) background, assigning a positive (negative) unit to each.

Our aim is to apply all of these quantities to obtain, in an accurate way, a morphological characterization of the different geometrical patterns described in Sec. II and, thus, characterize the transition induced by the control parameter in our system.

IV. RESULTS

We analyze the simulations performed in Sec. II, consisting on a set of Turing patterns ranging from white spots (islands) to black spots (holes) with their corresponding intermediate labyrinth patterns. In this section we present the morphological analysis in order to evaluate the transition due to the control parameter.

Figure 3(a) shows the value of the area, A^w, as a function of the control parameter, Θ. This functional increases with the forcing because the white area is occupying more surface up

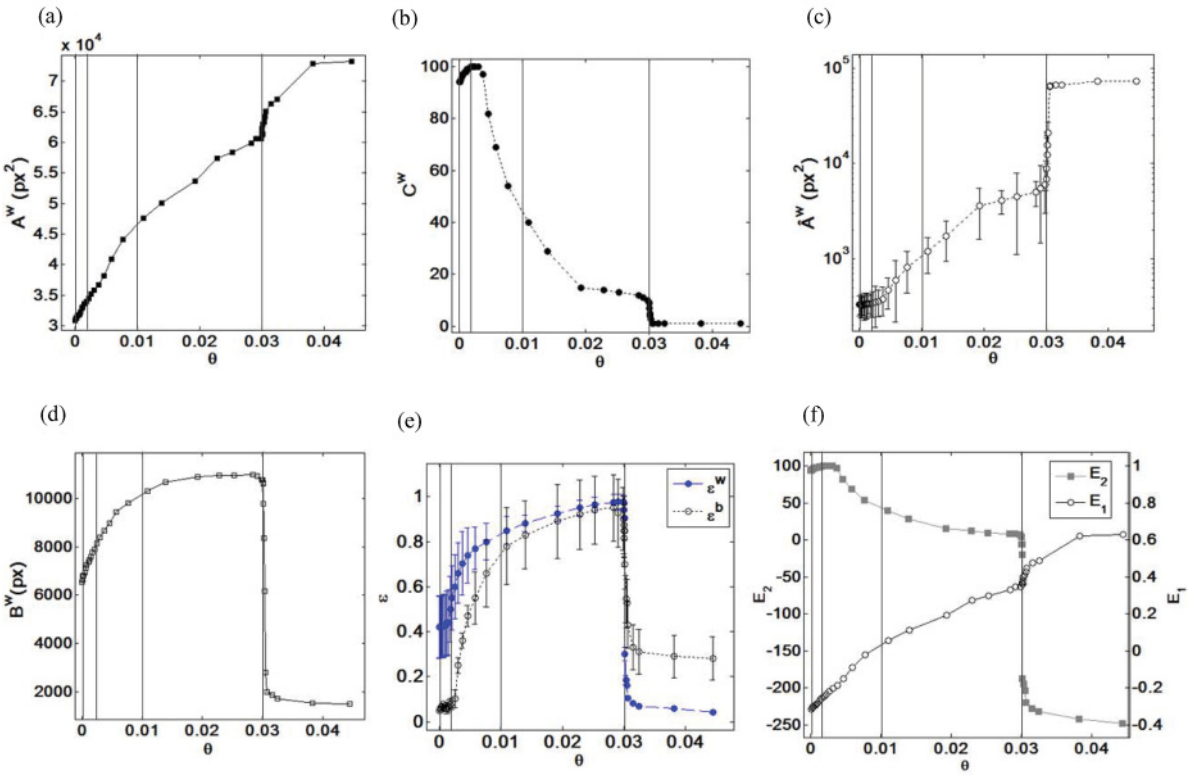

FIG. 3. (Color online) Variations of the morphological measures with the control parameter Θ. (a) The white area, A^w. (b) The number of clusters C^w. (c) The mean area per cluster, $\hat{A}^w$, in logscale, with dispersion, (d). The boundary length, B. (e) The mean eccentricity of black and white clusters (ε^w and ε^b, respectively) with their respectively uncertainties. (f) The Euler numbers, E_1 and E_2.

to a maximum value (81.33% of the total area, obtained in the black-spots regime). The area relates the growing of the pattern with the forcing but is not a good indicator to establish the pattern transitions.

In Figs. 3(b) and 3(c), we show the cluster distribution, C^w, with the forcing, and the mean area per cluster ($\hat{A}^w = A^w/C^w$) with its standard deviation, respectively. For low values of forcing the cluster distribution increases mainly due to the sharp reduction in the Turing wavelength observed in the white-spots regime. Therefore, the clusters are formed closer to each other, and, consequently, more clusters are taken into account in the analyzed domain due to the finite size of the images. For larger values of the control parameter, the presence of labyrinthine structures reflects an exponential decrease of the cluster distribution [from 100 to 10 clusters, see Fig. 3(b)] until the control parameter induces a sharp transition to black spots (this is at $\Theta = 0.03$). Higher values of the control parameter within the black-spots regime (i.e., $0.03 < \Theta < 0.045$) do not alter the type of pattern and induce only smooth changes in the wavelength, which have no measurable effects in the cluster distribution, remaining constant at $C^w = 1$. The mean area per cluster, $\hat{A}^w$, takes a low value for the labyrinthine structures until black spots appear for, i.e., $\Theta = 0.03$, as shown in Fig. 3(c). Note that the uncertainty of the distribution is smaller for low values of the forcing because most of the clusters are white spots. But, as we approach to the transition point, the white spots deform into labyrinths and the cluster distribution becomes more irregular. However, above this point, the sharp transition transforms the cluster distribution in only one great cluster, whose area is much larger than the others.

Figure 3(d) presents the boundary length, B, which is a much more sensitive magnitude to the transitions analyzed than the area. Different patterns exhibit different values for the boundary length while the area contained remains almost unchanged.

White spots or islands ($\Theta = 0$) present a boundary length smaller than the labyrinthine structures ($\Theta = 0.01$–0.03). From $\Theta = 0$ to 0.01, this functional grows linearly with the forcing, while in the labyrinthine range remains almost unaltered. Above $\Theta = 0.03$, the boundary length falls sharply due to the abrupt transition between labyrinth to black spots. This curve is not perfectly symmetric due to two main factors: (i) the wavelength decreases [as shown in Fig. 1(e)], producing a boundary length for the white spots larger than the observed for the black spots, and (ii) the response of the system to the perturbation is nonlinear.

The latest morphological measures are the eccentricity, ε^w, and the Euler numbers, $E_{1,2}$. The eccentricity is a mean value for each cluster, so we can obtain an uncertainty out of the distribution. This measure is related to the boundary length. Thus, in our system, patterns with larger boundary length imply a greater eccentricity. This is the reason because the boundary length and ε^w curves look so similar. In Fig. 3(e), at low forcing values we observe an eccentricity close to 0.4. Moreover, these results present a high uncertainty basically due to the appearance of small defects in the white spots, as an intermediate state before labyrinthine structures.

By smoothly increasing the forcing, in this regime ($0.0025 < \Theta < 0.007$), the ε^w measure exhibits a direct relation with the control parameter, reaching values up to twice the free-forcing case, i.e., around 0.8. This sharp increment in the eccentricity is related with the increasing number of labyrinthine irregularities. Above $\Theta = 0.008$ the labyrinthine configuration prevails over the white spots, resulting in an ε^w tending slowly to 1 and in decreasing the uncertainty. Once again, the forcing associated with the appearance of black spots ($\Theta = 0.03$) demonstrates a sharp decreasing in the eccentricity, falling down to 0.1. This value is smaller than the obtained for the white spots. The explanation is that the black-spots pattern looks like a white square with black holes, and the ellipse associated with the second central momentum of a square structure is close to 0. In addition, in order to elucidate these transitions, around $\Theta = 0.0025$ and $\Theta = 0.03$, we calculate the black-clusters eccentricity [dotted curve in Fig. 3(e)], i.e., ε^b. For low forcing values, ε^b is close to 0 (due to the presence of one black square cluster with white holes), further increasing the forcing, ε^b tends to 1 (stripes regime) and then it falls sharply to 0.34 (ε^b obtained for the black spots).

The Euler numbers, E_1 and E_2, are shown in Fig. 3(f). White spots (low forcing) present a low connectivity, i.e., $E_2 = 100$, due to the fact that the white clusters (or *islands*) are mainly disconnected between them. Furthermore, E_1 also presents a negative value, indicating that the black area dominates over the white one. At intermediate values of the control parameter, close to $\Theta = 0.01$, E_1 reaches the zero value, which corresponds with the transition from direct to reverse structures (the white area begins to be larger than the black area). Moreover, at $\Theta = 0.03$ the number of disconnected clusters (E_2) decreases to 0. This result suggests that the pattern changes from labyrinths to black spots (only one great white cluster). Moreover, in this transition point, E_2 reaches 200 holes due to the wavelength decrement.

Figure 4 shows all normalized measures described above. A cursory inspection points out the relationship between them, A^w with E_1, C^w with E_2, and B with ε^w, and how they are able to differentiate direct from reverse structures or the white spots from black and labyrinth. Thus, we expect that a combination of these quantities may account for all the different types of

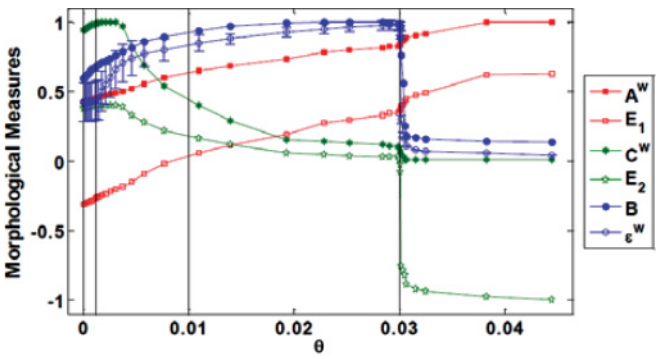

FIG. 4. (Color online) Comparison of all measures normalized. The normalization was performed by dividing over the maximum absolute value of each measure, i.e., $|A^w|_{\max} = 7.32 \times 10^4$ pixels^2, $|B|_{\max} = 1.09 \times 10^4$ pixels, $|C^w|_{\max} = 100$, $|E_2|_{\max} = 248$; the other measures are already normalized.

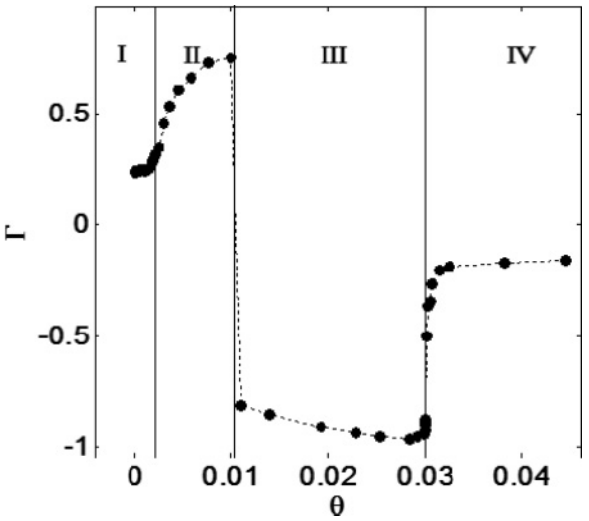

FIG. 5. Turing pattern transitions induced by the perturbation Θ. The Γ parameter discriminates among the different pattern configurations. Regions I (IV) and II (III) correspond to direct (reverse) patterns, white (black) spots and white (black) stripes, respectively.

patterns. We propose the following parameter defined as:

$$\Gamma = -\bar{\varepsilon}\,\mathrm{sgn}\,(E_1)\,, \tag{6}$$

where $\bar{\varepsilon}$ is the mean eccentricity between ε^w and $\varepsilon^{\cdot,b}$. With such a definition, the Γ parameter is able to differentiate between round and narrow clusters due to the eccentricity and, by means of E_1, between direct and reverse structures. According to this, the Γ parameter is able to distinguish among the patterns described in Sec. II A, as shown in Fig. 5. Note the sharp transitions delimiting the four different regimes. In this way, Γ discriminates four well-differentiated regions corresponding to the different types of patterns. In regions I and II, $\Gamma > 0$ indicates the presence of direct structures, i.e., white spots or white stripes. In region I the small value of Γ indicates that the structures are circlelike or white spots. When entering in region II ($\Theta = 0.0025$), Γ increases sharply until 0.8, indicating that the pattern evolves into a white-stripes structure. Around $\Theta = 0.01$, inverse structures dominate, $\Gamma < 0$, and the pattern evolves to black stripes described by a large value of Γ. And, finally, the last transition occurs at $\Theta = 0.03$, where the forcing transforms the black-stripes structures into black spots; note that Γ parameter falls to -0.2 due to the low eccentricity of the black spots. This parameter also describes the transient regimes before stationary patterns are fully established (see Appendix A).

In order to emphasize the relevance of the Γ parameter, we introduce a different system endowed with an internal dynamics such that it never reaches a stationary state but instead periodically oscillates between different configurations. In Fig. 7 we present experiments showing the temporal evolution of a CDIMA reaction subjected to a different spatiotemporal external forcing [25].

Basically, the system undergoes a periodic oscillation between two hexagonal-like Turing patterns. The experimental context can be followed in Refs. [24,25] and it implies a symmetry breaking phenomena leading to the alternation

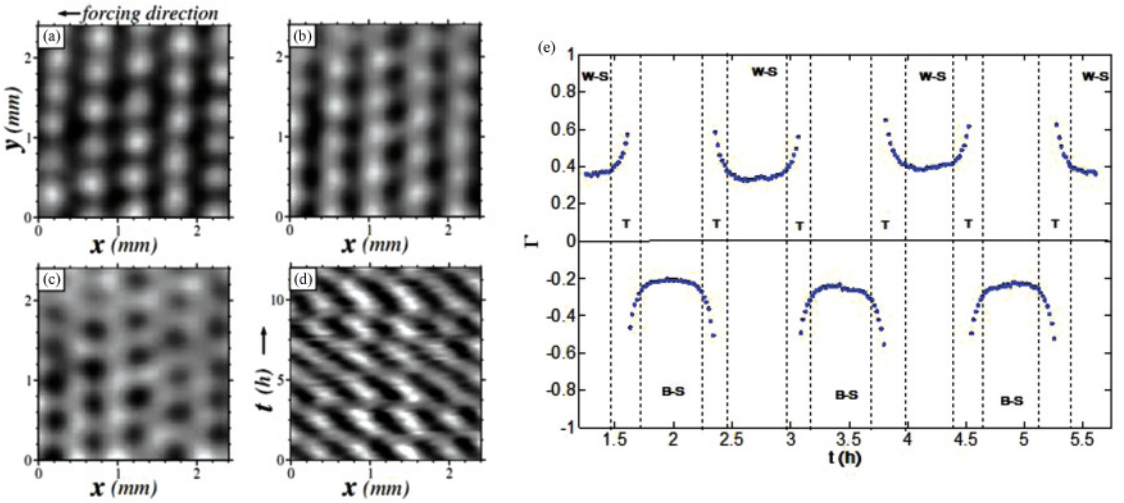

FIG. 6. (Color online) Temporal evolution of a forcing CDIMA reaction (courtesy of D. G. Míguez [25]). (a) White spots (W-S); (b) intermediate transition state (T); (c) black-spots (B-S). (d) Space-time plot of corresponding oscillations. (e) Oscillations of the Γ parameter with time (in hours).

between direct and reverse hexagons, i.e., white spots, W-S [Fig. 6(a)], and black spots, B-S [Fig. 6(c)], respectively. Transitions to a mixed state composed by black and white spots coexisting together appear for a short time [Fig. 6(b)], which makes them difficult to characterize at that time. The oscillatory dynamic is shown in the spatiotemporal plot in Fig. 6(d). From the complete temporal evolution we calculated the Γ parameter at each time and plotted its dependence with time in Fig. 6(e).

Note that the Γ parameter jumps from positive to negative values as the system transits from white to black spots. Additionally, the Γ parameter allows us to characterize the exact time where the mixed state exists (that periodically appears every 0.72 h).

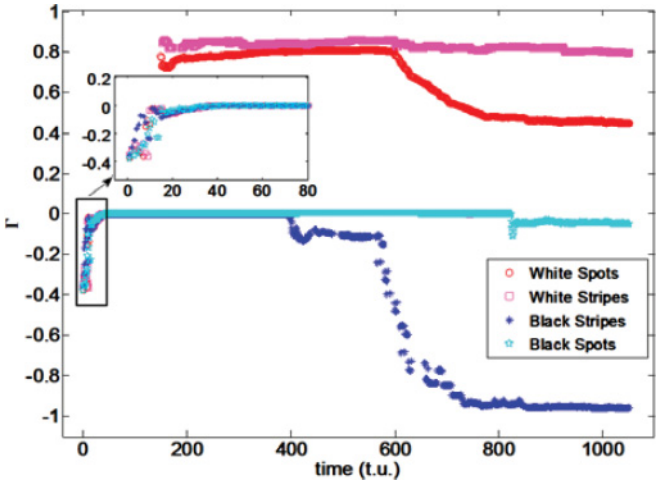

FIG. 7. (Color online) Temporal Evolution of Γ parameter for Turing patterns showed in Figs. 2(a)–2(d): white spots $\Theta = 0$ (red circles), white stripes $\Theta = 0.008$ (pink squares), black stripes $\Theta = 0.025$ (blue diamonds), and black spots $\Theta = 0.045$ (cyan stars). Simulations were performed with a time step of 10^{-4} t.u.

V. DICUSSION AND CONCLUSIONS

The morphological characterization of transitions between spatiotemporal structures is an interesting issue for diverse disciplines, in particular for nonlinear dynamics. In this work, we considered a theoretical and numerical example where Turing patterns present transitions among four different main structures from a morphological point of view. Due to the failure of the Fourier transform to account for this information, we apply the morphological measures that keep the entire structural description.

We analyzed a set of parameters known as the Minkowski functionals, as well as other morphological measures, to evaluate the topology and geometric characteristics of the Turing patterns and, in particular, the transitions between the different types of structures. We studied the variation of each functional with the control parameter, observing a great sensitivity to the perturbation. Further, the functionals present important correlations among them. Therefore, it is possible to define a sort of measure able to differentiate all types of Turing structures and characterize their transitions, $\Gamma = -\varepsilon^w \operatorname{sgn}(E_1)$. We observed two second-order phase transitions (in analogy with thermodynamic systems [44]) between spots and labyrinth structures and one first-order phase transition between direct and reversed structures.

In this paper we have applied the Γ functional to different examples coming from completely different contexts such as experiments with chemical reactions, numerical simulations, and patterns in nature (see Appendix B). In all cases, the Γ parameter is a useful tool to discriminate among the different morphological patterns. To conclude, the authors want to enhance the relevance of this morphological study as a useful technique to identify morphology and characterize possible transitions among a great diversity of dynamical spatiotemporal structures.

ACKNOWLEDGMENTS

This work was supported by the Ministerio de Educación y Ciencia and Xunta de Galicia under Research Grants

No. FIS2010-21023 and No. PGIDIT07PXIB-206077PR. J.C.-L. was supported by the MICINN under an FPI grant and J.G.-S. by a grant from the Xunta de Galicia.

APPENDIX A: TRANSIENT EVOLUTION OF PATTERNS

We analyze in this appendix the transient evolution of the system described in Sec. II before reaching the stationary states shown in Fig. 1.

The temporal evolution of the Γ parameter (Fig. 7) discriminates among the four different types of Turing patterns. Departing from initial random conditions, the Γ parameter gives us information about the precise moment at which we distinguish between black and white structures and also when the patterns reach the transient state. Thus, after a random initially state (see the inset in Fig. 7), the Γ parameter exhibits a bifurcation. Meanwhile, white patterns exhibit a strong increase in Γ (up to 0.8), with reverse structures presenting a constant value. Later, the Γ parameter also differentiates between spot and stripe configurations, demonstrating four different asymptotical solutions once the system reaches the transient.

APPENDIX B: CHARACTERIZATION OF PATTERNS IN NATURE

The Γ parameter is useful to characterize structures more complex than those patterns appearing in the CDIMA or BZ-AOT reactions. Here we consider the patterns spontaneously exhibited on the skin of animals (Fig. 8). Following the same procedure as described along this manuscript, we can calculate the Γ functional for the four examples plotted in Fig. 8. Reversepatterns (tiger and leopard skins) produce a negative value of Γ, while the *Ancistrus* fish and zebra present direct patterns and, therefore, the Γ value is positive. Furthermore, the numerical Γ values are compatible with those obtained for the numerical or experimental cases. This emphasizes the usefulness of this parameter to characterize patterns in completely different contexts.

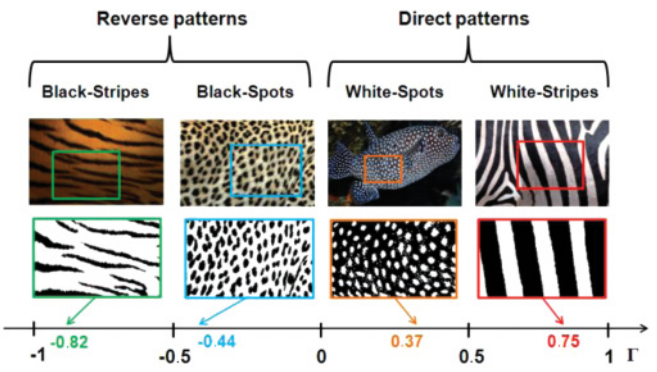

FIG. 8. (Color online) Morphological characterization of skin patterns. The first row presents direct pictures from animals (tiger, leopard, *Ancistrus* fish, and zebra). The second row are the corresponding digitalized images following the Otsu algorithm. The tiger and leopard skin patterns are reverse structures (with Γ equal to −0.82 and −0.44, respectively), while the fish (*Ancistrus*) and zebra skin are direct patterns (with Γ equal to 0.37 and 0.75, respectively).

[1] A. M. Turing, Philos. Trans. R. Soc. London B **237**, 37 (1952).
[2] S. Kondo and R. Asai, Nature **376**, 765 (1995).
[3] L. S. Schulman and P. E. Seiden, Science **233**, 425 (1986).
[4] J. Lechleiter, S. Girard, E. Peralta, and D. Clapham, Science **252**, 123 (1991).
[5] R. Kapral and K. Showalter, *Chemical Waves and Patterns* (Kluwer Academic, Dordrecht, 1993).
[6] B. P. Belousov, in *Collected Abstracts on Radiation Medicine*, edited by A. V. Lebedinskii (Medgiz, Moscow, 1959).
[7] A. N. Zaikin and A. M. Zhabotinskii, Nature (London) **225**, 535 (1970).
[8] V. K. Vanag and I. R. Epstein, Science **294**, 835 (2001).
[9] V. K. Vanag and I. R. Epstein, Phys. Rev. Lett. **92**, 128301 (2004).
[10] M. Kærn, R. Satnoianu, A. P. Muñuzuri, and M. Menzinger, Phys. Chem. Chem. Phys. **4**, 1315 (2002).
[11] B. Peña, C. Pérez-García, A. Sanz-Anchelergues, D. G. Míguez, and A. P. Muñuzuri, Phys. Rev. E **68**, 056206 (2003).
[12] David G. Míguez, S. Alonso, Alberto P. Muñuzuri, and F. Sagués, Phys. Rev. Lett. **97**, 178301 (2006).
[13] P. De Kepper, V. Castets, E. Dulos, and J. Boissonade, Physica D **49**, 161, (1991).
[14] V. K. Vanag and D. V. Boulanov, J. Phys. Chem. **98**, 1449 (1994).
[15] V. K. Vanag and I. R. Epstein, Science **294**, 835 (2001).
[16] V. K. Vanag and I. R. Epstein, Phys. Rev. Lett. **90**, 098301 (2003).
[17] J. Carballido-Landeira, I. Berestein, P. Taboada, V. Mosquera, V. K. Vanag, I. R. Epstein, V. Pérez-Villar, and A. P. Muñuzuri, Phys. Chem. Chem. Phys. **10**, 1094 (2008).
[18] I. P. Nagy and J. A. Pojman, J. Phys. Chem. **97**, 3443 (1993).
[19] J. Carballido-Landeira, V. K. Vanag, and I. R. Epstein, Phys. Chem. Chem. Phys. **12**, 3656 (2010).
[20] S. Rüdiger, D. G. Míguez, A. P. Muñuzuri, F. Sagués, and J. Casademunt, Phys. Rev. Lett. **90**, 128301 (2003).
[21] V. Pérez-Villar, J. L. F. Porteiro, and A. P. Muñuzuri, Phys. Rev. E **74**, 046203 (2006).
[22] G. Fernández-García, D. I. Roncaglia, V. Pérez-Villar, A. P. Muñuzuri, and V. Pérez-Muñuzuri, Phys. Rev. E **77**, 026204 (2008).
[23] A. von Kameke, F. Huhn, G. Fernández-García, A. P. Muñuzuri, and V. Pérez-Muñuzuri, Phys. Rev. E **81**, 066211 (2010).
[24] S. Rüdiger, D. G. Míguez, A. P. Muñuzuri, F. Sagués, and J. Casademunt, Phys. Rev. Lett. **90**, 128301 (2003).
[25] D. G. Míguez, E. M. Nicola, A. P. Muñuzuri, J. Casademunt, F. Sagués, and L. Kramer, Phys. Rev. Lett. **93**, 048303 (2004).
[26] H. Minkowski, Volumen and Oberfläche, Math. Ann. **57**, 447 (1903).

[27] H. Minkowski, Theorie der konvexen Körper, insbesondere Begründung ihres Oberflächenbegriffs, Vol. 2 (Gesammelte Abhandlungen, Leipzig, 1911).
[28] K. R. Mecke, Phys. Rev. E **53**, 4794 (1996).
[29] J. Serra, *Image Analysis and Mathematical Morphology* (Academic Press, London, 1982).
[30] A. Rosenfeld and A. C. Kak, *Digital Picture Processing* (Academic, New York, 1976).
[31] C. Likos, K. R. Mecke, and H. Wagner, J. Chem. Phys. **102**, 9350 (1995).
[32] K. R. Mecke, T. Buchert, and H. Wagner, Astron. Astrophys. **288**, 697 (1994).
[33] K. R. Mecke and H. Wagner, J. Stat. Phys. **64**, 843 (1991).
[34] V. K. Vanag, Usp. Fiz. Nauk **174**, 991 (2004).
[35] J. Guiu-Souto, J. Carballido-Landeira, A. P. Muñuzuri, and V. Pérez-Villar, Phys. Rev. E **82**, 066209 (2010).
[36] I. R. Epstein and V. K. Vanag, Chaos **15**, 047510 (2005).
[37] A. Kaminaga, V. K. Vanag, and I. R. Epstein, J. Chem. Phys. **122**, 174706 (2005).
[38] A. Kaminaga, V. K. Vanag, and I. R. Epstein, Angew. Chem. Int. Ed. **118**, 3159 (2006).
[39] J. Guiu-Souto, J. Carballido-Landeira, and A. P. Muñuzuri, Journal of Physics: Conference Series **296**, 0120156 (2011).
[40] K. Huang, *Statistical Mechanics* (John Wiley & Sons, Boston, 1987).
[41] F. Ames William, *Numerical Methods for Partial Differential Equations* (Academic Press, New York, 1977).
[42] N. Otsu, IEEE Transactions on Systems, Man, and Cybernetics **9**, 62 (1979).
[43] R. M. Haralick and L. G. Shapiro, *Computer and Robot Vision*, Vol. I (Addison-Wesley, New York, 1992).
[44] D. K. Kondepudi, *Introduction to Modern Thermodynamics* (John Wiley & Sons, Chichester, England, 2008).